



Simulation of ray-traced fringes and Zernike-based reconstruction of elliptical optical surfaces

Title	Simulation of ray-traced fringes and Zernike-based reconstruction of elliptical optical surfaces
Author(s)	Ibrahim, Dahi Ghareab Abdelsalam;Devaney, Nicholas
Publication Date	2026-02-06
Publisher	Optica Publishing Group
Repository DOI	https://doi.org/10.1364/AO.580581



Simulation of ray-traced fringes and Zernike-based reconstruction of elliptical optical surfaces

DAHI GHAREAB ABDELSALAM IBRAHIM^{1,2,*} AND NICHOLAS DEVANEY¹

¹*Applied Optics Group, Physics Unit, School of Natural Sciences, University of Galway, Galway, Ireland*

²*Engineering and Surface Metrology Laboratory, National Institute of Standards, Terna St., El Haram, El Giza, Egypt*

**dahi.ibrahim@universityofgalway.ie*

Received 30 September 2025; revised 16 January 2026; accepted 18 January 2026; posted 20 January 2026; published 6 February 2026

This study presents a comprehensive modeling and reconstruction framework for high-precision elliptical mirrors using simulated fringe patterns and Zernike polynomial fitting. A synthetic elliptical surface is generated, featuring a dome-shaped curvature with a radius of -1300 mm, major and minor axes of 229 and 124 mm, respectively, and sub-wavelength flatness and roughness characteristics. The surface is divided into 180 radial profiles using the non-interpolated profile rotation model (N-IPRM), which preserves native spatial sampling. To address discontinuities inherent in radial reconstruction, the interpolated profile rotation model (IPRM) applies shape-preserving interpolation to enable smooth surface recovery. Sag and slope equations derived from the interpolated profiles are used in a custom ray-tracing algorithm to simulate interference fringes at both visible (0.0006328 mm) and millimeter-wave (5.052296 mm) wavelengths. The algorithm incorporates planar, spherical, and oppositely curved spherical reference surfaces relative to the elliptical surface. The simulated fringe patterns undergo thinning and fringe order estimation, followed by surface reconstruction using a custom Zernike polynomial fitting algorithm implemented in MATLAB. Due to the challenges posed by incomplete circular fringes in Zernike-based reconstruction of elliptical surfaces, we propose a novel approach, to our knowledge: transforming the elliptical surface into an equivalent spherical surface, performing the reconstruction, and then converting it back to the original elliptical form. The reconstructed surface shows excellent agreement with the model, achieving an absolute error of 0.0161 mm and a relative error of 0.32% along the major axis at the longer wavelength. Symmetry deviations of approximately 0.5% further validate the reconstruction accuracy. This methodology provides a robust and versatile toolset for the simulation, analysis, and precise reconstruction of elliptical optical surfaces, with significant implications for optical fabrication and metrology.

Published by Optica Publishing Group under the terms of the [Creative Commons Attribution 4.0 License](https://creativecommons.org/licenses/by/4.0/). Further distribution of this work must maintain attribution to the author(s) and the published article's title, journal citation, and DOI.

<https://doi.org/10.1364/AO.580581>

1. INTRODUCTION

Elliptical shapes, due to their high precision and superior quality compared to spherical surfaces, offer significant advantages in optical systems, including improved imaging performance, wider fields of view, simplified designs, and reduced overall costs [1,2]. Consequently, elliptical optics are increasingly regarded as essential components in applications such as space optics, optical inspection systems, and smart devices [3,4]. Various manufacturing methods for elliptical surfaces, each with specific advantages and limitations, have been discussed in [4]. In this study, we model and reconstruct an elliptical surface with a radius of curvature of -1300 mm, a major axis of 229 mm, a minor axis of 124 mm, an RMS flatness of 77.5 nm, and an RMS surface roughness of 0.5 nm. The surface is generated

using the standard ellipse equation [5], combined with a dome-shaped curvature model [6]. To simulate realistic conditions, flatness and roughness noise components are added. The 2D elliptical surface is divided into 180 radial profiles, starting at 0° on the major axis and proceeding counterclockwise to 180° . These profiles are extracted using the non-interpolated profile rotation model (N-IPRM), which preserves the native spatial sampling by avoiding interpolation. Each profile is fitted with a second-degree polynomial to obtain sag equations, and the corresponding slopes are derived via analytical differentiation. Surface reconstruction begins with the simulation of interference fringes across the 2D elliptical surface using a custom ray-tracing algorithm, which takes both the fitted sag equations and their first derivatives as input. The algorithm models fringe formation by comparing the elliptical surface against planar,

spherical, and oppositely curved spherical reference surfaces. This ray-tracing process produces 180 one-dimensional intensity and phase profiles at two wavelengths: 0.0006328 mm (visible light) and 5.052296 mm (millimeter wave). The longer wavelength lies within the millimeter-wave band, typically ranging from 1 to 10 mm [7]. While N-IPRM provides accurate spatial sampling, its main limitation is the reconstruction of discrete radial lines rather than a continuous surface. To overcome this, we introduce the interpolated profile rotation model (IPRM), which employs shape-preserving piecewise cubic Hermite interpolation (PCHIP) [8]. This method preserves the local shape and monotonicity of the original profile, resulting in a smoother and more continuous surface reconstruction, especially beneficial when handling irregular data. Due to large sag values (in mm), fringe density is extremely high at the visible wavelength, with approximately 15,968.066 fringes along the major axis and 4526.094 fringes along the minor axis. At the longer wavelength, fringe density decreases significantly to about 20 and 5.669 fringes, respectively. Numerous methods exist for elliptical surface reconstruction [9,10], each with distinct trade-offs. In this work, we employ a custom Zernike polynomial-based reconstruction algorithm, implemented in MATLAB to reconstruct the 3D elliptical surface from the simulated fringes. A key advantage of Zernike polynomial fitting is that it requires only a single interferogram and eliminates the need for phase unwrapping algorithms [11,12]. This algorithm uses a 48-term expansion and incorporates fringe thinning to extract surface height information from the interpolated low-density fringe map. To address surface height overestimation caused by incorrect fringe order detection, we propose a novel approach: transforming the elliptical surface into an equivalent spherical surface, performing the reconstruction, and then converting it back to the original elliptical form. We begin by initializing a matrix of the same size as the major axis, extracting the 1D intensity profile along this axis, and applying the N-IPRM model with a circular mask. Rotating this profile from 0° to 180° produces a 2D intensity map representing a circular fringe pattern. A fringe thinning algorithm is then applied to extract the skeletons of the fringes, resulting in 20 circular fringes along both X and Y axes. These are labeled and numbered, with the spacing between successive fringes equal to half the wavelength. The Zernike polynomial fitting algorithm is then applied to reconstruct the 3D surface from the thinned and labeled fringes. An ellipse is subsequently overlaid on the reconstructed surface in the X-Y plane, defined parametrically as $X = a \cos(\theta)$, $Y = b \sin(\theta)$, where $a = 114.5$ mm and $b = 62$ mm are the semi-major and semi-minor axes, respectively, and $\theta \in [0, 2\pi]$. Data within this elliptical region are extracted for visualization and analysis. The reconstructed surface closely matches the simulated surface, yielding an absolute error of 0.016135 mm along the X axis and a relative error of 0.32%. Symmetry percentages are also computed: approximately 0.5% along the major axis and 1.3% along the minor axis. The lower error and higher symmetry along the major axis indicate better reconstruction accuracy, while the increased error along the minor axis is attributed to factors such as its shorter span, fewer data points, and higher discretization error near the edges. Overall, the proposed methodology provides a

robust framework for the modeling, simulation, and reconstruction of elliptical mirror surfaces, offering valuable insights for both optical manufacturing and performance assessment.

2. MODELING AN ELLIPTICAL MIRROR SURFACE WITH A 229 mm MAJOR AXIS, A 124 mm MINOR AXIS, A 77.5 nm RMS FLATNESS, AND A 0.5 nm RMS SURFACE ROUGHNESS

The simulation models an elliptical mirror surface with the following specifications: a major axis of 229 mm, a minor axis of 124 mm, 77.5 nm RMS flatness, and 0.5 nm RMS surface roughness. The mirror exhibits a large dome curvature, overlaid with low-frequency flatness noise and high-frequency surface roughness noise. The elliptical mirror has the following semi-axes: semi-major axis $a = 229/2 = 114.5$ mm and a semi-minor axis $b = 124/2 = 62$ mm. A 2D Cartesian grid is constructed over the bounding box, and a binary mask identifies the elliptical region using the standard ellipse equation [5]:

$$\frac{X^2}{a^2} + \frac{Y^2}{b^2} \leq 1. \quad (1)$$

Inside this ellipse, the mirror surface has a dome shape, which can be described by the spherical sag equation [6]:

$$Z_{\text{dome}}(x, y) = R - \sqrt{R^2 - x^2 - y^2}, \quad (2)$$

where R is the radius of curvature of the dome. In this simulation, $R = -1300$ mm. The surface is then vertically shifted so that the minimum sag within the ellipse is zero: $Z_{\text{dome}}(x, y) = Z_{\text{dome}}(x, y) - \min(Z_{\text{dome}}(x, y))$. To simulate low-frequency flatness errors, 2D Gaussian-filtered random noise is generated over the surface. The target RMS value for the flatness noise is $\text{RMS}_{\text{flat}} = 77.5$ nm. A random field is generated such that $\text{flat}_{\text{noise}}(x, y) \sim N(0, 1)$. This noise is zeroed outside the ellipse and smoothed with a Gaussian filter to simulate low-frequency behavior. The filtered noise is then scaled to achieve the desired RMS using: $\text{scale} = \text{overscale} \times (\text{RMS}_{\text{flat}}/\text{RMS}_{\text{current}})$. To simulate surface roughness, white Gaussian noise is added, such that $\text{rough}_{\text{noise}}(x, y) \sim N(0, 1)$. This noise is zeroed outside the ellipse and then scaled to the desired RMS value of 0.5 nm. The scaling is given by: $\text{rough}_{\text{noise}} = \text{rough}_{\text{noise}} \times (\text{RMS}_{\text{rough}}/\text{RMS}_{\text{current}})$. For the combined flatness and roughness noises, denoted $N_{\text{flat+rough}}$, the final RMS is computed as

$$\text{RMS}_{\text{flat}} = \sqrt{\frac{1}{N} \sum_{i=1}^N (N_{\text{flat+rough}})_i^2}, \quad (3)$$

and the PV of the total noise is computed as

$$\text{PV} = \max(N_{\text{flat+rough}}) - \min(N_{\text{flat+rough}}). \quad (4)$$

The total simulated mirror surface is the sum of the dome, flatness noise, and roughness noise:

$$z_T(x, y) = z_{\text{dome}}(x, y) + \text{flat}_{\text{noise}}(x, y) + \text{rough}_{\text{noise}}(x, y). \quad (5)$$

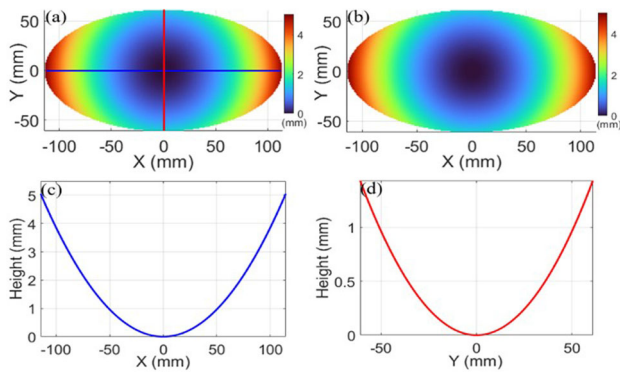


Fig. 1. (a) Two-dimensional map of the ideal elliptical mirror surface. (b) Two-dimensional map of the elliptical mirror surface with added noise. (c) Cross-sectional profile along the X axis of (a). (d) Cross-sectional profile along the Y axis of (a).

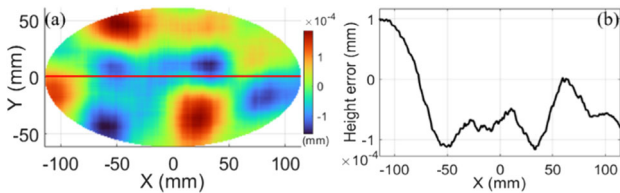


Fig. 2. (a) Two-dimensional noise error map. (b) Cross-sectional profile along the X axis of (a).

All noise components are constrained to within the elliptical mask. The grid spans from $-a = -114.5$ mm to $+a = +114.5$ mm along the X direction and from $-b = -62$ mm to $+b = +62$ mm along the Y direction.

With a grid spacing of 1 mm, this results in 230 pixels along the X axis and 125 pixels along the Y axis. Therefore, the grid consists of 125×230 pixels, covering a physical area of 124×229 mm², with each pixel representing an area of 1×1 mm². The Gaussian filter is applied using `imgaussfilt` with a standard deviation of $\sigma = 15$ mm. This means that the low-frequency flatness noise is smoothed over spatial scales of approximately 15 mm, effectively suppressing high-frequency variations and simulating large-scale surface figure errors. Figure 1(a) shows a 2D pure elliptical mirror surface simulated using Eq. (5) without flatness noise and roughness noise. Figure 1(b) shows the 2D noisy elliptical mirror surface simulated using Eq. (5) with both flatness and roughness noise. The added noise is relatively small compared to the maximum sag, which is 5.052296 mm along the X axis and 1.432056 mm along the Y axis. Figures 1(c) and 1(d) show the cross-sectional profiles along the X axis and Y axis of Fig. 1(a), respectively. Figure 2(a) shows the 2D noise error $N_{\text{flat+rough}} = (\text{flat}_{\text{noise}} + \text{rough}_{\text{noise}})$, obtained by subtracting Figs. 1(a) and 1(b). This process ensures that the RMS of $N_{\text{flat+rough}}$ is 77.501 nm. Figure 2(b) shows the cross-sectional profile along the X axis of Fig. 2(a).

3. RECONSTRUCTION OF AN ELLIPTICAL SURFACE USING THE N-IPRM

To reconstruct the elliptical surface shown in Fig. 1(b), 180 diameter profiles of the surface sag (height) are extracted, each oriented at a distinct angle θ_i , where $\theta_i = \frac{i\pi}{179}$, $i = 0, 1, \dots, 179$. Each profile corresponds to a linear cross-section through the ellipse center at angle θ_i . The maximum radial extent along this line, denoted as $R(\theta_i)$, depends on the ellipse's shape and orientation and is computed as

$$R(\theta_i) = \frac{ab}{\sqrt{(b \cos \theta_i)^2 + (a \sin \theta_i)^2}} \quad (6)$$

The full diameter of the profile at angle θ_i is $D_i = 2R(\theta_i)$. Due to the elliptical geometry, each profile has a different length D_i , resulting in a variable number of sampled points n_i . Instead of interpolating all profiles onto a uniform spatial grid, the non-interpolated profile rotation model (N-IPRM) retains each profile's native sampling and length. For each profile i , the radial coordinate $t_{i,k}$ is defined over its natural range as

$$t_{i,k} = -R(\theta_i) + \frac{2R(\theta_i)}{n_i - 1} (k - 1), \quad k = 1, 2, \dots, n_i. \quad (7)$$

The coordinate $t_{i,k}$ starts at $-R(\theta_i)$ (the left end) and ends at $+R(\theta_i)$ (the right end), with uniform spacing between points. These radial positions are then converted to Cartesian coordinates for each sampled point:

$$X_{i,k} = t_{i,k} \cos \theta_i, \quad Y_{i,k} = t_{i,k} \sin \theta_i, \quad (8)$$

and the corresponding sag (height) values $Z_{i,k}$ are taken directly from the profile data. This approach generates a scattered set of 3D points $(X_{i,k}, Y_{i,k}, Z_{i,k})$ without enforcing uniform spatial sampling or interpolation between profiles. The reconstructed surface is visualized as a scatter plot of discrete points, preserving the original sampling of the simulated or measured data. The primary advantage of this method is that it maintains the true spatial sampling of the input profiles without distortion from resampling or interpolation. Figure 3(a) shows the reconstructed elliptical surface from Fig. 1(b) using the non-interpolated profile rotation model (N-IPRM). Figure 3(b) presents a subset of 20 radial profiles located within the white wedge region highlighted in Fig. 3(a). The main limitation of this model is that the reconstructed surface appears as discrete lines rather than a continuous surface, as illustrated in Fig. 3(b). To address this issue, we employed the interpolated profile rotation model (IPRM), which enables smooth surface reconstruction through interpolation.

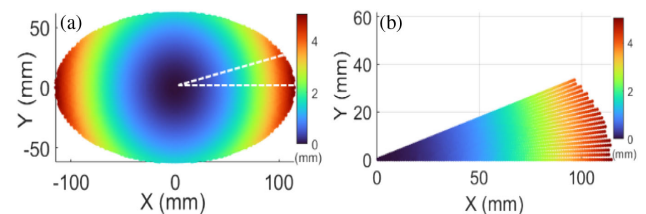


Fig. 3. (a) Reconstruction of the elliptical surface from Fig. 1(b) using the non-interpolated profile rotation model (N-IPRM). (b) Subset of 20 radial profiles extracted from the white wedge region highlighted in (a).

4. RECONSTRUCTION OF AN ELLIPTICAL SURFACE USING THE IPRM

Using the same profile orientations and radius computations defined in Eq. (6), each profile has a full diameter $D_i = 2R(\theta_i)$. Due to the elliptical geometry, these diameters vary with angle θ_i , and the corresponding profiles consist of n_i points sampled non-uniformly along their respective diameters. To enable consistent surface reconstruction on a common spatial grid, each profile is resampled through interpolation. The process begins by selecting a global diameter D (typically the largest among all D_i) to define a uniform spatial coordinate $d \in [-\frac{D}{2}, \frac{D}{2}]$, discretized into N_d equally spaced points:

$$d_j = -\frac{D}{2} + \frac{(j-1)D}{N_d-1}, \quad j = 1, 2, \dots, N_d \quad (9)$$

Each original profile is sampled along its native coordinate:

$$d_{i,k} = -\frac{D_i}{2} + \frac{(k-1)D_i}{n_i-1}, \quad k = 1, 2, \dots, n_i \quad (10)$$

To align all profiles onto a common radial grid d_j , each individual profile $Z_i(d_{i,k})$, originally sampled at its own radial positions $d_{i,k}$, is interpolated using shape-preserving piecewise cubic Hermite interpolation (PCHIP). This method constructs a smooth curve through the original data points while preserving the local shape and monotonicity of the profile. Unlike the standard cubic splines, which can introduce unwanted oscillations, PCHIP ensures that the interpolated curve does not overshoot and closely follows the original profile's trends. The interpolation is applied using MATLAB's `interp1` function as follows:

$$Z_i^{\text{interp}}(d_j) = \text{interp1}(d_{i,k}, Z_i(d_{i,k}), d_j). \quad (11)$$

This produces a new version of each profile Z_i^{interp} evaluated on the shared grid d_j , enabling consistent comparison and surface reconstruction across all profiles. Points outside the valid range $[-D_i/2, D_i/2]$ are typically assigned zero values or excluded during visualization. Next, a 2D polar grid is created using the angles θ_i and the uniform coordinates d_j . Each point on the grid is then converted to Cartesian coordinates:

$$X_{j,i} = d_j \cos \theta_i, \quad Y_{j,i} = d_j \sin \theta_i. \quad (12)$$

The corresponding interpolated sag values are as follows:

$$Z_{j,i} = Z_i^{\text{interp}}(d_j). \quad (13)$$

The result is a regular grid of points $(X_{i,k}, Y_{i,k}, Z_{i,k})$ that defines the reconstructed elliptical surface. This surface can be visualized as a continuous 3D mesh (e.g., using MATLAB's `surf` function), enabling smooth shading and analysis.

The main advantage of this approach is that it facilitates uniform surface representation and visualization, especially when the original profile data are irregular or sparse. Figure 4(a) shows the reconstructed elliptical surface from Fig. 1(b) using the interpolated profile rotation model (IPRM), and Fig. 4(b) shows a subset of 20 radial profiles within the white wedge region of Fig. 4(a). Figure 5(a) shows the radial profiles corresponding to rotation angles from 0° to 90° , while Fig. 5(b)

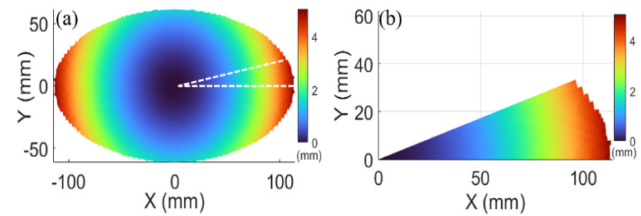


Fig. 4. (a) Reconstruction of the elliptical surface from Fig. 1(b) using the interpolated profile rotation model (IPRM). (b) Subset of 20 radial profiles extracted from the white wedge region shown in (a).

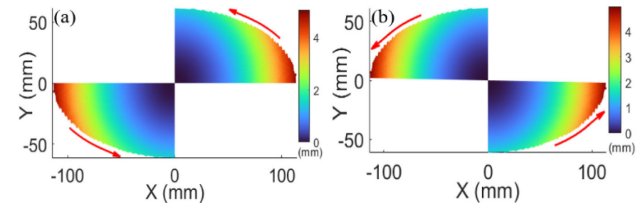


Fig. 5. Application of the interpolated profile rotation model (IPRM) to the reconstructed surface in Fig. 4(a), showing radial profiles corresponding to rotation angles from (a) 0° to 90° and (b) 90° to 180° .

displays profiles from 90° to 180° . Conceptually, the reconstructed surface can be divided into two halves: the rotation from 0° to 90° covers quadrants 1 and 3, whereas the rotation from 90° to 180° spans quadrants 2 and 4.

5. RAY-TRACED ELLIPTICAL FRINGE SIMULATION USING A CUSTOM RAY-TRACING ALGORITHM

A. Case Study: Using Planar Surface 2 as a Reference

In this paper, a simulated elliptical surface is ray-traced using a custom ray-tracing algorithm to generate interference fringes at each point on the surface. The program traces rays through a multi-surface optical system in 2D. Figure 6(a) shows the actual surfaces plotted using IDL software, with surface 3 generated using Eq. (14). In contrast, Fig. 6(b) displays the same surfaces, but with surface 3 generated using Eq. (16). Surfaces 1, 2, and 4 are planar and defined by linear equations, whereas surface 3 is an elliptical profile plotted from the 180 sag values $Z_{i,k}$ extracted from Fig. 1(b), evaluated at each orientation angle θ_i . Since the ray-tracing algorithm requires both the sag equations and their derivatives, each of the 180 sag profiles $Z_{i,k}$ is fitted with a second-degree polynomial. This fitting process provides both the analytical sag equations and their corresponding first derivatives (slopes). As a result, 180 sag equations and their associated slope functions are generated. These sag equations and their derivatives are then used as inputs to the custom ray-tracing algorithm, which is developed to simulate interference fringes.

The algorithm processes all 180 profiles one by one to generate the corresponding one-dimensional intensity and phase maps of the elliptical surface at two wavelengths: 0.0006328 and 0.5052296 mm. Surface 3 in Fig. 6(a) corresponds to profile_000, which achieves a sag of 5.052296 mm along the X axis.

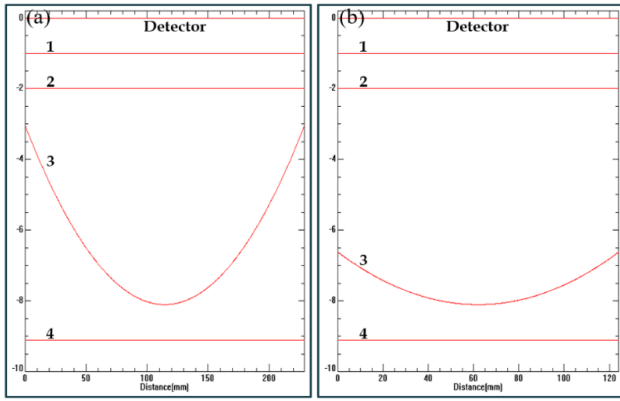


Fig. 6. Actual surfaces plotted using the IDL software: (a) Surface 3 generated from Eq. (14) and (b) surface 3 generated from Eq. (16).

The sag equation for profile_000 is given by

$$z_0 = 3.8532 \times 10^{-4}x^2 - 8.8238 \times 10^{-2}x + 5.0506. \quad (14)$$

Its first derivative (slope) is given by

$$z'_0 = 7.7064 \times 10^{-4}x - 8.8238 \times 10^{-2}. \quad (15)$$

Surface 3 in Fig. 6(b) corresponds to profile_090, which achieves a sag of 1.432056 mm along the Y axis. The sag equation for profile_090 is given by

$$z_{90} = 3.8531 \times 10^{-4}x^2 - 4.7784 \times 10^{-2}x + 1.4809. \quad (16)$$

Its first derivative is given by

$$z'_{90} = 7.7063 \times 10^{-4}x - 4.7784 \times 10^{-2}. \quad (17)$$

Rays are modeled as straight lines in the $x - y$ plane, and their interactions (reflections and transmissions) with optical surfaces are computed accordingly. A ray is described by the parametric equations: $x = x_0 + l \sin(a)$, $y = y_0 + l \cos(a)$, where (x_0, y_0) is the initial position of the ray, a is the angle of incidence, and l is the distance traveled by the ray. The angle a is expressed in radians and computed using: $a_i = \pi - \frac{2\pi - \alpha}{360}$, where $\alpha = 0.01^\circ$. Rays propagate through the optical system and interact with multiple surfaces. The initial ray spacing is set to 0.001 mm, and any rays with amplitudes below 0.01 are discarded. Upon encountering a surface, the ray's behavior depends on the refractive indices of the involved media and the reflection/transmission coefficients. For reflected rays, the angle of reflection is given by $a_r = \pi - a_i$. For transmitted rays, Snell's Law is applied: $n_1 \sin(a_i) = n_2 \sin(a_t)$, where n_1 and n_2 are refractive indices, and a_i and a_t are the angles of incidence and transmission, respectively. For a ray directed toward a surface defined by $y = f(x)$, the intersection point (x_{next}, y_{next}) is calculated as: $x_{next} = x_0 + l \sin(a)$ and $y_{next} = y_0 + l \cos(a)$. Given the previous point (x_{in}, y_{in}) and current point (x, y) , the traveled distance is $l = \sqrt{(x - x_{in})^2 + (y - y_{in})^2}$. The optical path length is updated using: $pathlength_{new} = pathlength_{old} + l \cdot n$, where n is the refractive index of the medium. The traveled distance l is computed and added to the existing path length. This accumulated optical path length is then used to compute the phase as follows:

$$\phi = \frac{2\pi}{\lambda} \cdot pathlength + phase\ shifts. \quad (18)$$

The intensity pattern is computed over discrete pixels with a size of 10 μm using the following formula [13]:

$$I = \sum (A \cos(\phi))^2 + \sum (A \sin(\phi))^2. \quad (19)$$

The ray amplitude A is updated as it propagates through the system, accounting for Fresnel reflection and transmission at each interface, as well as cumulative attenuation. The corresponding phase pattern is calculated as

$$\Phi = \tan^{-1} \left[\frac{\sum A \sin(\phi)}{\sum A \cos(\phi)} \right]. \quad (20)$$

The clear aperture of the simulated elliptical surface in Fig. 1(b) is 124 mm along the minor axis and 229 mm along the major axis. The elliptical surface consists of 180 sag profiles, each represented by its own fitted sag equation and corresponding derivative. For profile_000 (aligned with the major axis), 229,000 rays are traced, and for profile_090 (aligned with the minor axis), 124,000 rays are traced. The average number of rays per profile is approximately $(229,000 + 124,000)/2 \approx 177,000$. This results in a total of $180 \times 177,000 = 31,860,000$ rays. Approximately 32 million rays are traced in total.

For each profile, the ray-tracing computation takes about 30 min on a laptop equipped with an Intel i5 CPU @ 2.21 GHz and 16 GB of RAM. As a result, 180 intensity profiles and 180 phase profiles are generated at a wavelength of 0.0006328 mm, according to Eqs. (19) and (20), respectively. The non-interpolated profile rotation model (N-IPRM) is applied to these profiles to reconstruct the 2D intensity map, as shown in Fig. 7(a), with cross-sectional intensity profiles along the X and Y axes presented in Figs. 7(b) and 7(c), respectively. The same N-IPRM procedure is used to generate the 2D phase map in Fig. 8(a), with the corresponding cross-sectional phase profiles along the X and Y axes shown in Figs. 8(b) and 8(c), respectively. As shown in Fig. 7, the high-density fringes observed at a wavelength of 0.0006328 mm arise from the surface sag. Along the X profile, the maximum sag is 5.052296 mm, which corresponds to the number of fringes (NOFs) calculated as $NOF = 5.052296 \text{ mm} / 0.0006328 \text{ mm} \approx 7984.033$ fringes. Considering the two sags across the 2D elliptical surface, the total number of fringes is $NOF_{total} = 2 \times 7984.033 = 15968.066$ fringes. Similarly, along the Y profile, the maximum sag is 1.432056 mm, resulting in $NOF = 1.432056 \text{ mm} / 0.0006328 \text{ mm} \approx 2263.047$ fringes, and the total number of fringes across the 2D elliptical surface is calculated as: $NOF_{total} = 2 \times 2263.047 = 4526.094$ fringes.

To reduce the fringe count along the X axis to approximately 20, the same elliptical surface was retraced using a longer wavelength of 0.5052296 mm. The number of fringes (NOF) along the X axis is calculated as $NOF = 5.052296 \text{ mm} / 0.5052296 \text{ mm} = 10$ fringes.

Therefore, considering both sags along the X axis, the total number of fringes is $NOF_{total} = 10 \times 2 = 20$ fringes. For the Y axis, the fringe count is $NOF = 1.432056 \text{ mm} / 0.5052296 \text{ mm} = 2.835$ fringes. Thus,

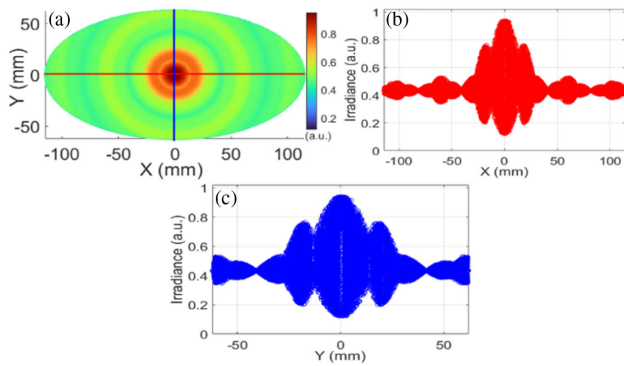


Fig. 7. (a) Two-dimensional intensity map of the simulated elliptical surface from Fig. 1(b), obtained at a wavelength of 0.0006328 mm. (b) Cross-sectional intensity profile along the X axis of (a). (c) Cross-sectional intensity profile along the Y axis of (a).

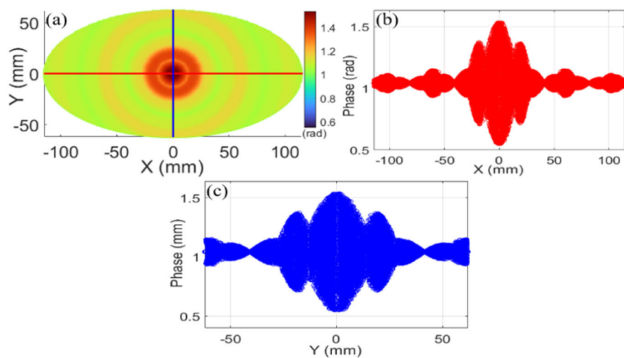


Fig. 8. (a) Two-dimensional phase map of the simulated elliptical surface shown in Fig. 1(b), obtained at a wavelength of 0.0006328 mm. (b) Cross-sectional phase profile along the X axis of (a). (c) Cross-sectional phase profile along the Y axis of (a).

across both sags along the Y axis, the total number of fringes is $\text{NOF}_{\text{total}} = 2.835 \times 2 = 5.669$ fringes. Note that the X axis corresponds to profile_000 and the Y axis corresponds to profile_090. After extracting the 180 fitted sag equations and their derivatives from Fig. 1(b), each equation and derivative were processed sequentially using the ray-tracing algorithm at the wavelength of 0.5052296 mm. This procedure generated 180 intensity profiles and 180 phase profiles according to Eqs. (19) and (20), respectively. The non-interpolated profile rotation model (N-IPRM) was then applied to reconstruct the 2D intensity map, as shown in Fig. 9(a). Figures 9(b) and 9(c) present the cross-sectional intensity profiles along the X axis and Y axis of Fig. 9(a), respectively. As shown in Fig. 9(b), the total number of fringe counts along the X axis and Y axis are approximately 20 and 5.669, respectively, consistent with the calculated values and validating the custom ray-tracing algorithm. Similarly, the N-IPRM was used to generate the 2D phase map displayed in Fig. 10(a), with corresponding cross-sectional phase profiles along the X axis and Y axis shown in Figs. 10(b) and 10(c), respectively. Since the intensity and phase maps in Figs. 9(a) and 10(a) are reconstructed using the N-IPRM, the resulting surfaces are inherently discrete, as discussed in Section 3.

To achieve continuous 2D surface reconstruction, the interpolated profile rotation model (IPRM) was applied to the 180

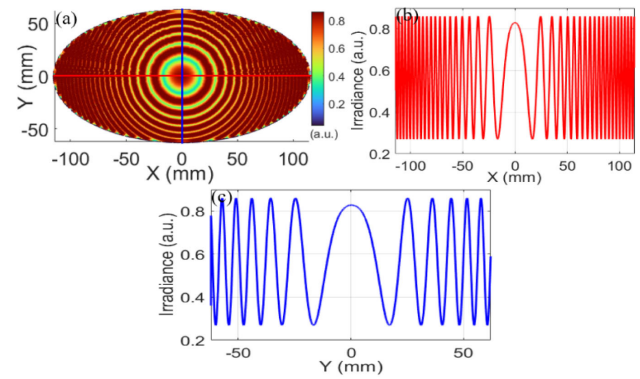


Fig. 9. (a) Two-dimensional intensity map of the simulated elliptical surface shown in Fig. 1(b), obtained at a wavelength of 0.5052296 mm using the non-interpolated profile rotation model (N-IPRM). (b) Cross-sectional intensity profile along the X axis of (a). (c) Cross-sectional intensity profile along the Y axis of (a).

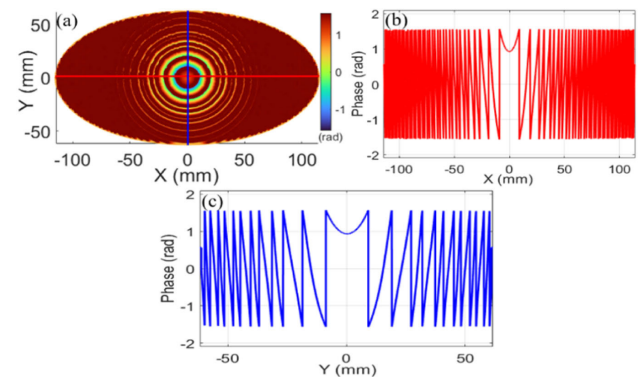


Fig. 10. (a) Two-dimensional phase map of the simulated elliptical surface shown in Fig. 1(b), obtained at a wavelength of 0.5052296 mm using the non-interpolated profile rotation model (N-IPRM). (b) Cross-sectional phase profile along the X axis of (a). (c) Cross-sectional phase profile along the Y axis of (a).

intensity and phase profiles obtained from ray-tracing the elliptical surface in Fig. 1(b), resulting in smooth, continuous intensity and phase maps. Figures 11(a) and 11(c) show the interpolated 2D intensity and phase maps, respectively, while Figs. 11(b) and 11(d) present the corresponding cross-sectional profiles along the X axis.

B. Case Study: Using Spherical Surface 2 as a Reference

Figures 12(a) and 12(b) present surface plots generated using the IDL software, where planar surface 2 from Fig. 6 is replaced with (a) a spherical surface having a curvature similar to that of surface 3 and (b) a spherical surface with curvature opposite to that of surface 3, respectively.

A typical one-dimensional fringe intensity profile and the corresponding 1D phase profile, generated using ray-tracing from the surfaces in Fig. 12(a), are shown in Figs. 13(a) and 13(b), respectively. As shown in Fig. 13(a), although the number of fringes remains fixed at 20, the intensity distribution across the fringes exhibits noticeable variation. The one-dimensional intensity profile shown in Fig. 13(a) is radially replicated using

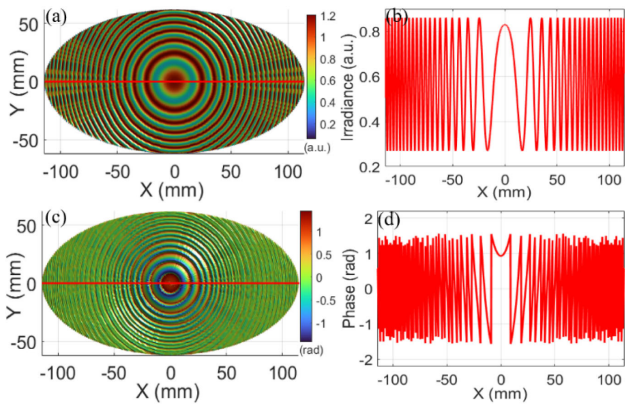


Fig. 11. (a) Two-dimensional interpolated intensity map of the simulated elliptical surface from Fig. 1(b), obtained at a wavelength of 0.5052296 mm using the interpolated profile rotation model (IPRM). (b) Cross-sectional intensity profile along the X axis of (a). (c) Two-dimensional interpolated phase map generated using the IPRM. (d) Cross-sectional phase profile along the X axis of (c).

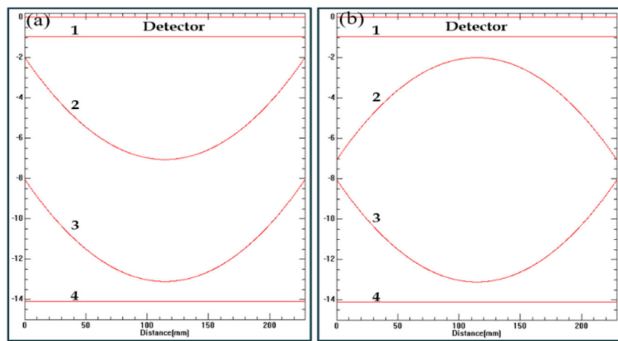


Fig. 12. Surface plots generated using the IDL software by replacing planar surface 2 from Fig. 6 with: (a) a spherical surface having a curvature similar to that of surface 3 and (b) a spherical surface with a curvature opposite to that of surface 3.

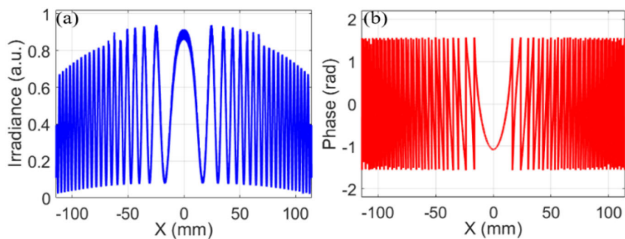


Fig. 13. (a) One-dimensional intensity profile and (b) the corresponding 1D phase profile, generated using ray-tracing from the surfaces shown in Fig. 12(a).

the non-interpolated profile rotation model (N-IPRM). A square matrix of size 229 mm × 229 mm is generated, where the elliptical mask from Eq. (1) is replaced by a circular mask of uniform radius defined by $X^2 + Y^2 \leq 114.5$, with 114.5 mm being the radius of the circle. The resulting two-dimensional circular intensity map is shown in Fig. 14(a).

A centrally overlaid ellipse is added to Fig. 14(a), lying in the X-Y plane and defined parametrically as $X = a \cos(\theta)$, $Y = b \sin(\theta)$, where $a = 114.5$ mm and $b = 62$ mm are the

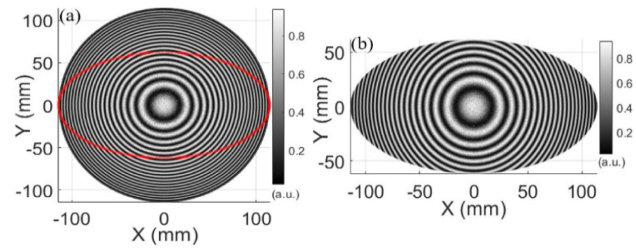


Fig. 14. (a) Two-dimensional circular intensity map generated by radially replicating the one-dimensional intensity profile from Fig. 13(a) using the N-IPRM, with an overlaid elliptical mask. (b) Extracted intensity data from within the elliptical region shown in (a).

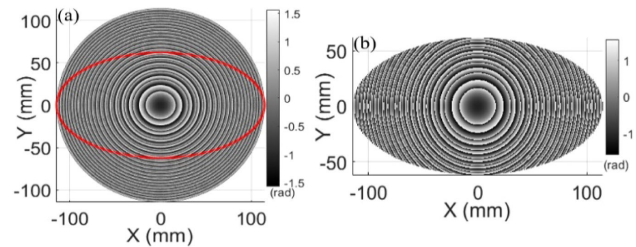


Fig. 15. (a) Two-dimensional circular phase map generated by radially replicating the one-dimensional phase profile from Fig. 13(b) using the N-IPRM, with an overlaid elliptical mask. (b) Extracted phase data from within the elliptical region shown in (a).

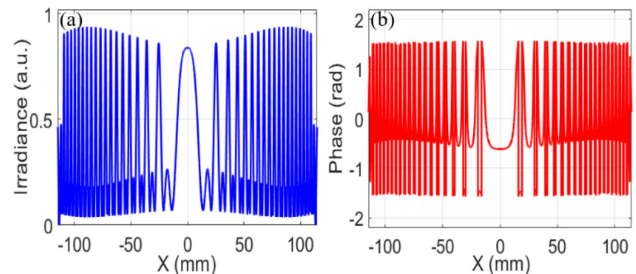


Fig. 16. (a) One-dimensional intensity profile generated by ray-tracing from the surfaces shown in Fig. 12(b). (b) One-dimensional phase profile generated by ray-tracing from the same surfaces in Fig. 12(b).

semi-major and semi-minor axes, respectively, and $\theta \in [0, 2\pi]$. The data within this elliptical mask in Fig. 14(a) are extracted and shown in Fig. 14(b).

Similarly, the one-dimensional phase profile shown in Fig. 13(b) is radially replicated using the N-IPRM. The resulting two-dimensional circular phase map is shown in Fig. 15(a), with the same centrally overlaid ellipse defined by $a = 114.5$ mm and $b = 62$ mm. The phase data inside this elliptical region are extracted and presented in Fig. 15(b). The one-dimensional intensity profile and the corresponding one-dimensional phase profile, generated using ray-tracing from the surfaces shown in Fig. 12(b), are presented in Figs. 16(a) and 16(b), respectively.

As shown in Fig. 16(a), the number of main fringes remains constant at 20, with each main fringe accompanied by smaller subsidiary fringes. The one-dimensional intensity profile shown

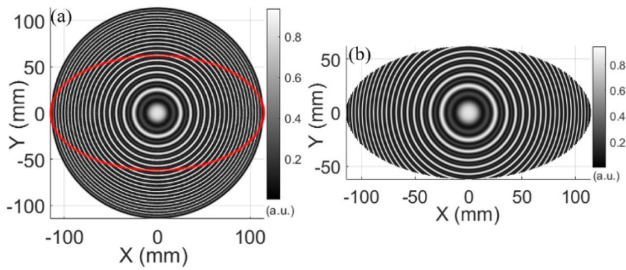


Fig. 17. (a) Two-dimensional circular intensity map generated by radially replicating the one-dimensional intensity profile from Fig. 16(a) using the N-IPRM, with a centrally overlaid elliptical mask. (b) Extracted intensity data from within the elliptical region shown in (a).

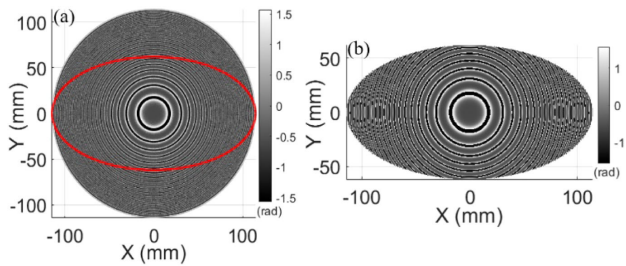


Fig. 18. (a) Two-dimensional circular phase map generated by radially replicating the one-dimensional phase profile from Fig. 16(b) using the N-IPRM, with a centrally overlaid elliptical mask. (b) Extracted phase data from within the elliptical region shown in (a).

in Fig. 16(a) is radially replicated using the non-interpolated profile rotation model (N-IPRM), replacing the elliptical mask from Eq. (1) with a circular mask of radius 114.5 mm. The resulting two-dimensional circular intensity map is shown in Fig. 17(a). An ellipse with semi-major axis $a = 114.5$ mm and semi-minor axis $b = 62$ mm is centrally overlaid on Fig. 17(a). The intensity data within this elliptical region are extracted and shown in Fig. 17(b). Similarly, the one-dimensional phase profile shown in Fig. 16(b) is radially replicated using the N-IPRM. The resulting two-dimensional circular phase map is shown in Fig. 18(a), with the same centrally overlaid ellipse defined by $a = 114.5$ mm and $b = 62$ mm. The phase data within this elliptical region are extracted and displayed in Fig. 18(b).

6. RECONSTRUCTION OF INTERPOLATED ELLIPTICAL FRINGE PATTERNS USING A CUSTOM ZERNIKE POLYNOMIAL FITTING ALGORITHM

The surface height function at any point of the exit pupil, $Z_r(x_r, y_r)$, can be represented as a linear combination of M polynomials $F(x_r, y_r)$ and their corresponding weighting coefficients G [14–16]:

$$Z_r(x_r, y_r) = \sum_{j=1}^M F_j(x_r, y_r) G_j, \tag{21}$$

where r is the sample index. Calculating these coefficients is essential for accurately representing the surface. This is accomplished by thinning and ordering the fringes, followed by fitting the data to a polynomial set. This process is typically performed using the least squares method [17], where S is defined as the sum of the squares of the differences between the data points and the fitted polynomial values:

$$S = \sum_{r=1}^N \left[Z_r - \sum_{j=1}^M G_j F_j(x_r, y_r) \right]^2. \tag{22}$$

In an ideal scenario, a perfect fit would yield $S = 0$, indicating no discrepancy between the measured data and the fitted polynomial. However, due to inherent surface irregularities and measurement noise, S is always nonzero. The goal of the least-squares fit is to determine the coefficients of the polynomial basis functions that minimize S . These coefficients are found by taking the partial derivative of S with respect to each coefficient and setting the result to zero. The resulting system of equations can be expressed in matrix form using summations:

$$\begin{bmatrix} \sum_{r=1}^N Z_r F_1(x_r, y_r) \\ \vdots \\ \sum_{r=1}^N Z_r F_M(x_r, y_r) \end{bmatrix} = \begin{bmatrix} \sum_{r=1}^N F_1(x_r, y_r) F_1(x_r, y_r) & \dots & \sum_{r=1}^N F_M(x_r, y_r) F_1(x_r, y_r) \\ \vdots & \ddots & \vdots \\ \sum_{r=1}^N F_1(x_r, y_r) F_M(x_r, y_r) & \dots & \sum_{r=1}^N F_M(x_r, y_r) F_M(x_r, y_r) \end{bmatrix} \times \begin{bmatrix} G_1 \\ \vdots \\ G_M \end{bmatrix} \tag{23}$$

A total of 48 coefficients G_j were calculated numerically, providing a complete representation of the surface. Figure 19(a) shows the grayscale version of the interpolated interferogram in Fig. 11(a). To isolate the bright fringe structures, the interferogram is thresholded by selecting all pixels with intensities greater than 63% of the maximum brightness. These pixels are set to 1 in a new binary image. A median filter with a window size of 8×8 is then applied to reduce noise in the binary fringe pattern. The resulting filtered image, converted to double precision, is shown in Fig. 19(b). Next, a fringe thinning algorithm [18] is applied to geometrically reduce the width of the binary fringes, effectively extracting their skeletons, as shown in Fig. 19(c). The thinned fringes are then labeled, with each assigned a distinct color, as illustrated in Fig. 19(d).

The total number of detected fringe regions in Fig. 19(d), including both continuous and disconnected segments, is 34. When the 34 thinned fringes in Fig. 19(c) are fitted using Zernike polynomial fitting, the reconstructed surface height is overestimated. This is because the fringe

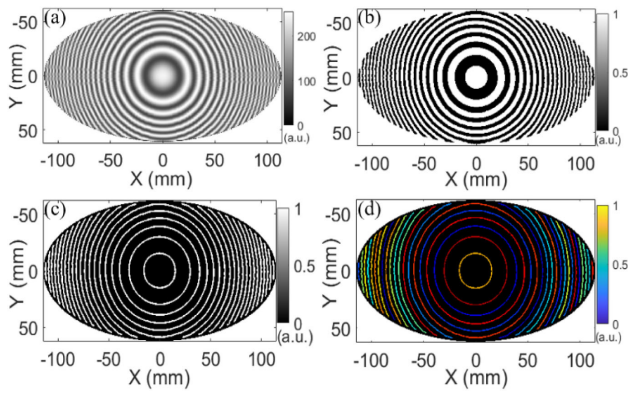


Fig. 19. (a) Grayscale version of the interpolated interferogram from Fig. 11(a). (b) Binary image obtained by thresholding at 63% of the maximum intensity to isolate bright fringes. (c) Thinned fringes extracted from (b) using skeletonization. (d) Labeled and color-coded thinned fringes from (c), with 34 detected fringes.

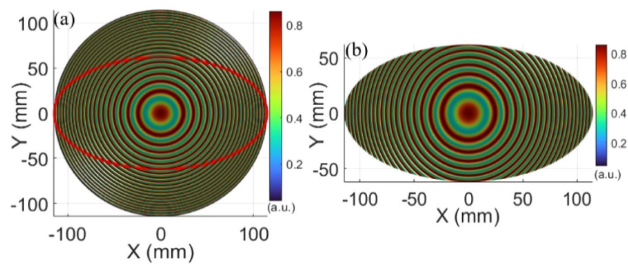


Fig. 20. (a) Two-dimensional circular fringe pattern generated over a 229 mm × 229 mm area with a centrally overlaid ellipse, produced using the N-IPRM. (b) Extracted fringe data within the elliptical region shown in (a).

count is 34 instead of the correct 20, leading to a calculated maximum height of approximately 8.59 mm ($34 \times 0.5052296 \text{ mm}/2$) $\approx 8.59 \text{ mm}$, whereas the actual height should be around 5.052 mm ($20 \times 0.5052296 \text{ mm}/2$) for 20 fringes. To resolve this discrepancy, a square matrix of size 229 mm × 229 mm, matching the major axis length, is created. Since the surface is rotationally symmetric, a 1D intensity profile along the X axis (the major axis) of Fig. 19(a) is radially replicated, replacing the elliptical mask in Eq. (1) with a circular mask of uniform radius defined by $X^2 + Y^2 \leq 114.5$, where 114.5 mm is the radius of the circle. Figure 20(a) shows the generated 2D circular fringe pattern over this area, with a centrally overlaid ellipse, defined parametrically by $X = a \cos(\theta)$, $Y = b \sin(\theta)$, where $a = 114.5 \text{ mm}$ and $b = 62 \text{ mm}$ are the semi-major and semi-minor axes, respectively, and $\theta \in [0, 2\pi]$.

The data within the overlaid ellipse in Fig. 20(a) are extracted and shown in Fig. 20(b). A fringe thinning algorithm was applied to Fig. 20(a), yielding the result shown in Fig. 21(a). An ellipse with a major axis of $2a = 229 \text{ mm}$ and a minor axis of $2b = 124 \text{ mm}$ was overlaid at the center of Fig. 21(a) and highlighted in red. The data within this elliptical region were extracted and are presented in Fig. 21(b). The resulting thinned fringes were then labeled, with each fringe assigned a distinct color, as shown in Fig. 22(a).

A total of 20 closed fringes were detected in Fig. 22(a). It is important to note that when the elliptical mask is applied to

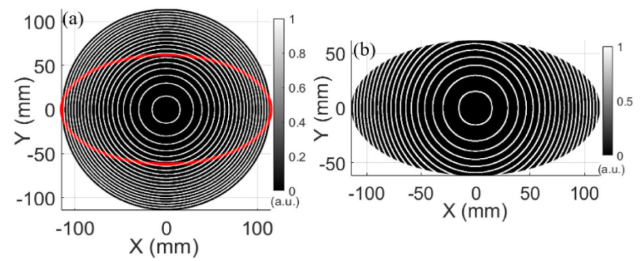


Fig. 21. (a) Thinned fringes obtained by applying a fringe thinning algorithm to the 2D circular fringe pattern shown in Fig. 20(a), with an overlaid ellipse. (b) Extracted fringe data confined within the elliptical region indicated in (a).

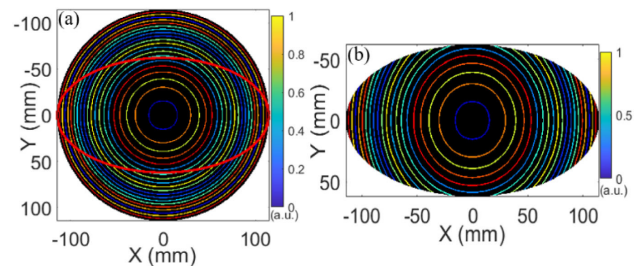


Fig. 22. (a) Labeled and color-coded thinned fringes derived from Fig. 21(a), with an overlaid ellipse. (b) Extracted data confined within the elliptical region shown in (a).

Fig. 22(a), the extracted data, shown in Fig. 22(b), are identical to those in Fig. 19(d), differing only in color representation. This confirms the correctness of the proposed method for reconstructing elliptical surfaces. Zernike polynomial fitting was applied to the 20 complete circular fringes shown in Fig. 22(a). The resulting reconstructed surface is presented in Fig. 23(a). An ellipse with a major axis of $2a = 229 \text{ mm}$ and a minor axis of $2b = 124 \text{ mm}$ was then centrally overlaid on Fig. 23(a) and highlighted in blue. The data within the overlaid ellipse in Fig. 23(a) were extracted and are presented in Fig. 23(b). Figures 24(a) and 24(b) present the cross-sectional profiles along the X axis and Y axis of Fig. 23(b), respectively. For the X profile shown in Fig. 24(a), the left and right sag differences are $\Delta_L = 5.093974 \text{ mm}$ and $\Delta_R = 5.042888 \text{ mm}$, respectively, yielding an average of $\bar{\Delta} = (\Delta_L + \Delta_R)/2 = 5.068431 \text{ mm}$. For the Y profile shown in Fig. 24(b), the left and right sag differences are $\Delta_L = 1.483680 \text{ mm}$ and $\Delta_R = 1.523164 \text{ mm}$, with an average of $\bar{\Delta} = 1.503422 \text{ mm}$.

These computed averages closely align with the actual sag values of 5.052296 mm for the X profile and 1.432056 mm for the Y profile. The absolute and relative errors are computed to quantify the deviation of the measured values from the actual values. The absolute error is defined as $|\text{measured value} - \text{actual value}|$, and the relative error is given by: $\text{relative error}(\%) = (|\text{measured-actual}|/|\text{actual}|) \times 100\%$. For the X profile, the absolute error is $|5.068431 - 5.052296| = 0.016135 \text{ mm}$, and the relative error is $(|5.068431 - 5.052296|/|5.052296|) \times 100\% \approx 0.32\%$. For the Y profile, the absolute error is $|1.503422 - 1.432056| = 0.071366 \text{ mm}$, and the relative error is $(|1.503422 - 1.432056|/|1.432056|) \times 100\% \approx 4.99\%$. The larger relative error observed in the Y profile can be primarily attributed to several factors.

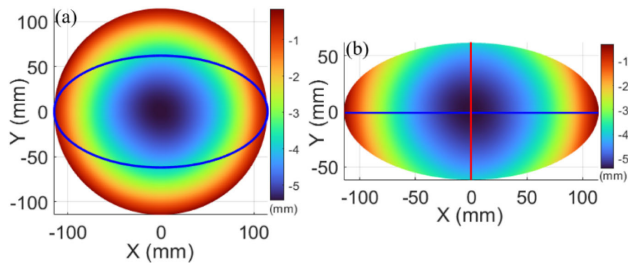


Fig. 23. (a) Reconstruction of the thinned fringes from Fig. 22(a) after applying Zernike polynomial fitting, with a centrally overlaid ellipse. (b) Data extracted from within the ellipse shown in (a).

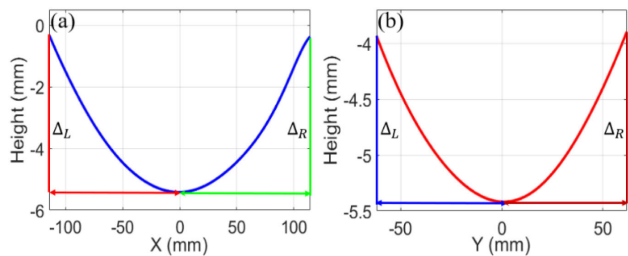


Fig. 24. Cross-sectional profiles extracted from Fig. 23(b) along the (a) X axis and (b) Y axis, respectively.

First, the Y profile spans a smaller physical range compared to the X profile, resulting in fewer data points and greater sensitivity to discretization errors. Second, masking outside the elliptical region affects the Y profile more significantly due to the shorter vertical axis. Finally, the use of 48 Zernike coefficients, while sufficient to capture the main curvature and medium-order surface variations, may not fully represent finer details along the minor axis. This limitation can cause slight asymmetry between the left and right sag values, contributing to the higher relative error and symmetry deviation observed in the Y profile.

To calculate σ_x and σ_y for Figs. 24(a) and 24(b), we evaluate the symmetry of the sag profiles [19]. The standard deviation σ quantifies how symmetric the sag profile is on either side of the center by measuring the spread of the left and right sag differences (Δ_L and Δ_R) from their average $\bar{\Delta}$. It is defined as

$$\sigma = \sqrt{\frac{(\Delta_L - \bar{\Delta})^2 + (\Delta_R - \bar{\Delta})^2}{2}}. \quad (24)$$

If σ is close to zero, the sag profile is nearly symmetric about the center, as the edge sag values deviate very little from the average. Conversely, a large σ relative to $\bar{\Delta}$ indicates asymmetry. Symmetry can also be expressed as a percentage using $(\sigma/\bar{\Delta}) \times 100\%$. A small percentage (e.g., <1%) indicates high symmetry, while a larger percentage implies greater asymmetry. For the X profile, the computed standard deviation is $\sigma_x \approx 0.02554$ mm, corresponding to a symmetry percentage of approximately 0.5%. For the Y profile, $\sigma_y \approx 0.01974$ mm, with a symmetry percentage of approximately 1.3%. The symmetry analysis of the reconstructed sag profiles indicates good overall reconstruction quality in both directions. The X profile exhibits a symmetry value of approximately 0.5%, which reflects a highly symmetric profile and demonstrates excellent agreement

between the left and right edge sag values. The Y profile shows a slightly higher symmetry value of approximately 1.3%; however, this remains within acceptable limits for elliptical surface reconstruction. The increased symmetry percentage in the Y direction can be attributed primarily to the shorter physical extent of the minor axis, which results in fewer effective data points and a smaller average sag value. Consequently, even small absolute deviations between the left and right sag values lead to a larger relative symmetry percentage. In addition, masking and edge effects outside the elliptical region have a more pronounced influence along the shorter vertical axis. These factors collectively explain the observed difference and confirm that the asymmetry in the Y profile arises from geometric and numerical considerations rather than deficiencies in the proposed reconstruction method.

7. CONCLUSION

This study presents a robust and high-precision framework for the modeling, simulation, and reconstruction of elliptical mirror surfaces using simulated interference fringes and custom Zernike polynomial fitting. A realistic elliptical surface, featuring dome-shaped curvature, flatness and roughness noise, and peak-to-valley height, was generated to emulate practical fabrication scenarios. The surface was divided into 180 radial profiles using the non-interpolated profile rotation model (N-IPRM) to preserve native spatial sampling, while the interpolated profile rotation model (IPRM) enabled smooth two-dimensional reconstruction via shape-preserving interpolation. Fringe patterns were simulated on the elliptical surface at visible and millimeter-wave wavelengths using a custom ray-tracing algorithm with various reference surfaces. The resulting one-dimensional fringe profiles were converted into two-dimensional intensity and phase maps, which were then reconstructed using a custom Zernike fitting algorithm. To address fringe-order ambiguity, a novel approach was applied by transforming the surface into a spherical domain for reconstruction and subsequently converting it back to elliptical coordinates. The final reconstruction closely matched the original surface, achieving an absolute error of 0.0161 mm and a relative error of 0.32% along the major axis, with symmetry deviations within 0.5%, demonstrating highly accurate surface reconstruction. These results confirm the accuracy and versatility of the proposed framework for applications in optical fabrication, metrology, and performance evaluation of elliptical optics. Future work may extend this approach to experimental validation using real-world fringe data.

Funding. Freeform Optix Disruptive Technologies Innovation Fund (DTIF) (DT20220389B (2023–2026); Irish Research eLibrary.

Acknowledgment. This research is conducted under Freeform Optix DT20220389B (2023–2026), funded under the Disruptive Technologies Innovation Fund (DTIF), a €500 million fund established under Project Ireland 2040, run by the Department of Enterprise, Trade and Employment, with administrative support from Enterprise Ireland. The opinions expressed by the authors are their own. Open access funding provided by Irish Research eLibrary.

Disclosures. The authors declare no conflicts of interest.

Data availability. Data underlying the results presented in this paper are not publicly available at this time but may be obtained from the authors upon reasonable request.

REFERENCES

1. J. Liu, *Elliptical Mirrors: Applications in Microscopy* (IOP Publishing, 2018).
2. C. Liu, G. E. Ice, W. Liu, *et al.*, "Fabrication of nested elliptical KB mirrors using profile coating for synchrotron radiation X-ray focusing," *Appl. Surf. Sci.* **258**, 2182–2186 (2012).
3. Q. Deng, Y. Wang, L. Sun, *et al.*, "A polishing method using self-excited oscillation abrasive flow for the inner surface of workpiece," *Int. J. Adv. Manuf. Technol.* **119**, 4093–4108 (2022).
4. M. Feng, Y. Lei, Z. Chen, *et al.*, "Whole elliptical surface polishing using a doughnut-shaped MCF polishing tool with variable tilt angle," *Lubricants* **10**, 232 (2022).
5. K. C. Zhou, A. Dhalla, R. P. McNabb, *et al.*, "High-speed multiview imaging approaching 4pi steradians using conic section mirrors: theoretical and practical considerations," *J. Opt. Soc. Am. A* **38**, 1810–1822 (2021).
6. Y. Yang, H. Hu, E. Qi, *et al.*, "Testing of spherical mirrors with extremely large R numbers using a quasi-autocollimation method," *Opt. Express* **32**, 22858–22877 (2024).
7. Y. Tamura, R. Kawabe, Y. Fukasaku, *et al.*, "Wavefront sensor for millimeter/submillimeter-wave adaptive optics based on aperture-plane interferometry," *Proc. SPIE* **11445**, 114451N (2021).
8. J. He, L. Yuan, H. Lei, *et al.*, "A novel piecewise cubic hermite interpolating polynomial-enhanced convolutional gated recurrent method under multiple sensor feature fusion for tool wear prediction," *Sensors* **24**, 1129 (2024).
9. L. Huang, T. Wang, F. Polack, *et al.*, "Measurement uncertainty of highly asymmetrically curved elliptical mirrors using multi-pitch slope stitching technique," *Front. Phys.* **10**, 880772 (2022).
10. S. J. Thompson, R. Lang, P. Röss, *et al.*, "Reconstruction of a conic-section surface from autocollimator-based deflectometric profilometry," *Appl. Opt.* **55**, 2827–2836 (2016).
11. D. G. A. Ibrahim, "Quantitative phase imaging using a combination of flat fielding and windowed Fourier filtering demodulated by graph cuts algorithm for screening opaque and transparent objects," *Opt. Continuum* **1**, 246–260 (2022).
12. D. G. A. Ibrahim, "3D shape reconstruction of normal and cancerous red blood cells using digital holographic tomography: combination of angular spectrum method and multiplicative technique," *J. Microsc.* **287**, 156–166 (2022).
13. M. Born and E. Wolf, *Principles of Optics: Electromagnetic Theory of Propagation, Interference and Diffraction of Light* (Cambridge University, 1999).
14. D. J. Fischer, J. T. O'Bryan, R. Lopez, *et al.*, "Vector formulation for interferogram surface fitting," *Appl. Opt.* **32**, 4738–4743 (1993).
15. J. Y. Wang and D. E. Silva, "Wave-front interpretation with Zernike Polynomials," *Appl. Opt.* **19**, 1510–1518 (1980).
16. D. G. Abdelsalam, M. S. Shaalan, M. M. Eloker, *et al.*, "Radius of curvature measurement of spherical smooth surfaces by multiple-beam interferometry in reflection," *Opt. Lasers Eng.* **48**, 643–649 (2010).
17. J. L. Rayces, "Least-squares fitting of orthogonal polynomials to the wave aberration function," *Appl. Opt.* **31**, 2223–2228 (1992).
18. T. Y. Zhang and C. Y. Suen, "A fast parallel algorithm for thinning digital patterns," *Commun. ACM* **27**, 236–239 (1984).
19. I. T. Nistea, S. G. Alcock, P. Kristiansen, *et al.*, "Long, elliptically bent, active X-ray mirrors with slope errors <math><200\text{ nrad}</math>," *J. Synchrotron Radiat.* **24**, 615–621 (2017).